

# CHS-Net: A Deep learning approach for hierarchical segmentation of COVID-19 infected CT images

Narinder Singh Punm<sup>a,\*</sup>, Sonali Agarwal<sup>a</sup>

<sup>a</sup>*Indian Institute of Information Technology Allahabad, Prayagraj, Uttar Pradesh, India*

---

## Abstract

The pandemic of novel severe acute respiratory syndrome coronavirus 2 (SARS-CoV-2) also known as COVID-19 has been spreading worldwide, causing rampant loss of lives. Medical imaging such as computed tomography (CT), X-ray, etc., plays a significant role in diagnosing the patients by presenting the visual representation of the functioning of the organs. However, for any radiologist analyzing such scans is a tedious and time-consuming task. The emerging deep learning technologies have displayed its strength in analyzing such scans to aid in the faster diagnosis of the diseases and viruses such as COVID-19. In the present article, an automated deep learning based model, COVID-19 hierarchical segmentation network (CHS-Net) is proposed that functions as a semantic hierarchical segmenter to identify the COVID-19 infected regions from lungs contour via CT medical imaging. The CHS-Net is developed with the two cascaded residual attention inception U-Net (RAIU-Net) models where first generates lungs contour maps and second generates COVID-19 infected regions. RAIU-Net comprises of a residual inception U-Net model with spectral spatial and depth attention network (SSD), consisting of contraction and expansion phases of depthwise separable convolutions and hybrid pooling (max and spectral pooling) to efficiently encode and decode the semantic and varying resolution information. The CHS-Net is trained with the segmentation loss function that is the weighted average of binary cross entropy loss and dice loss to penalize false negative and false positive predictions. The approach is compared with the recently proposed research works on the basis of standard metrics

---

\*Corresponding author

*Email addresses:* `pse2017002@iiita.ac.in` (Narinder Singh Punm ),  
`sonali@iiita.ac.in` (Sonali Agarwal)

like accuracy, precision, sensitivity, recall, F1 score, dice coefficient and Jaccard index. With extensive trials, it is observed that the proposed approach outperformed the recently proposed approaches and effectively segments the COVID-19 infected regions in the lungs.

*Keywords:* COVID-19, Coronavirus, CT images, Deep learning, Hierarchical segmentation, Medical imaging.

---

## 1. Introduction

The novel coronavirus, also known as COVID-19, is an on-going world-wide pandemic that initiated from Wuhan, the People's Republic of China in December 2019 and till December 10, 2020, have caused 68,894,596 infections and 1,569,374 deaths worldwide [1]. The exponential growing trend of COVID-19 is highlighted in Fig. 1 that shows the number of confirmed cases out of which 2% died and 64% recovered worldwide since the time it is recorded [2]. With the exponential spread of the virus, the World Health Organization (WHO) declared the coronavirus outbreak as a public health emergency of international concern (PHEIC) in January 2020 and later as pandemic in March 2020 [3]. This has raised the concern in every sector of the international community such as public health, transportation, marketing, tourism, manufacturing, lifestyle, etc. Even with various advancements in technology, unfortunately till now there is no concrete solution or medicine to cure COVID-19 and hence the international community is adopting the avoidance and preventive measures that involve self hygiene, no social contact, avoiding finger touch on the public doors, elevators, etc. [4]. Since COVID-19 is highly contagious, the infected ones are kept in isolation and closely monitored by the doctors and experts for treatment to minimize its spread. Moreover, the availability of resources of COVID-19 detection and diagnosis is quite limited as compared to its requirement, hence researchers are exploring all possible ways to detect and analyse the impact of infection on human body. With this motivation, biomedical image analysis have become prominent area of research to aid in the diagnosis of COVID-19.

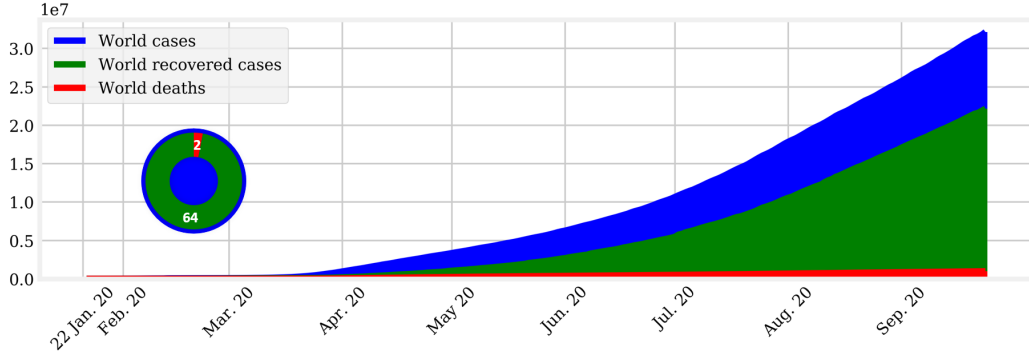


Figure 1: Exponential growth trend of COVID-19 worldwide.

In biomedical image analysis, the problems can be interpreted as classification and segmentation to identify and detect any abnormality in the radiography [5] via deep learning techniques, where the convolution neural network (CNN) based architectures are the most promising and popular choice in the research community. CNNs have displayed remarkable performance over the years and are being deployed for endoscopic videos [6], CT images [7], diagnosis of pediatric pneumonia using chest X-ray images [8, 9], etc. In the context of COVID-19, the classification task involves a prediction for the patient being infected with the virus in the presence of binary or multi-class samples [8, 10, 11] (involving other viruses or diseases than COVID-19), whereas in segmentation the coronavirus infected regions are localized and in-painted [12, 13] via lungs CT or X-ray imaging.

### 1.1. Why lungs segmentation?

Currently, reverse transcription-polymerase chain reaction (RT-PCR) test act as the standard to diagnose and confirm the symptoms of COVID-19 in any patient [14]. However, the RT-PCR assay is deficit to fulfil the demand in every area. The test takes around 4 to 6 hours and is less sensitive to confirm the coronavirus at the initial stages. The current findings indicate that COVID-19 affects various organs of a human being, such as blood vessels, heart, stomach, intestines, brain and kidneys [15]. The virus enters into the cells surface receptors angiotensin-converting enzyme 2 or ACE2 which is present on alveoli of the lungs. Therefore, lungs become the primary target for the virus affection which later spread to other body organs. Following

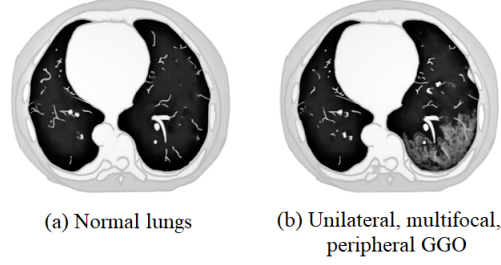


Figure 2: Chest CT imaging of normal and COVID-19 infected lungs.

from this context, computed tomography (CT) imaging of the human lungs is considered to diagnose and test the COVID-19 infections. It has been observed that bilateral, multifocal and peripheral ground glass opacification (GGO) that follows typical patterns, are predominant CT findings in patients suffering from COVID-19 [16] as highlighted in Fig. 2. However, for any radiologist analyzing CT scan is a time consuming and tedious task. Thus, biomedical image analysis techniques involving deep learning and machine learning algorithms are developed for faster cures and treatment.

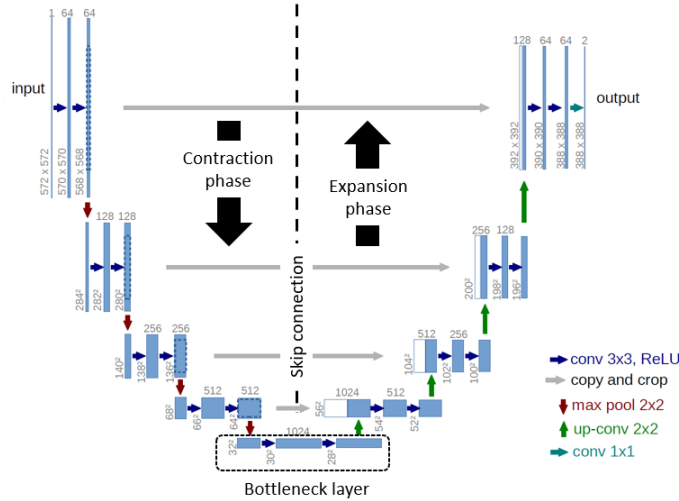


Figure 3: Schematic representation of base U-Net model.

### 1.2. U-Net

U-Net [17] model, as shown in Fig. 3, is the most extensively utilized CNN based deep learning architecture for medical image segmentation. Due

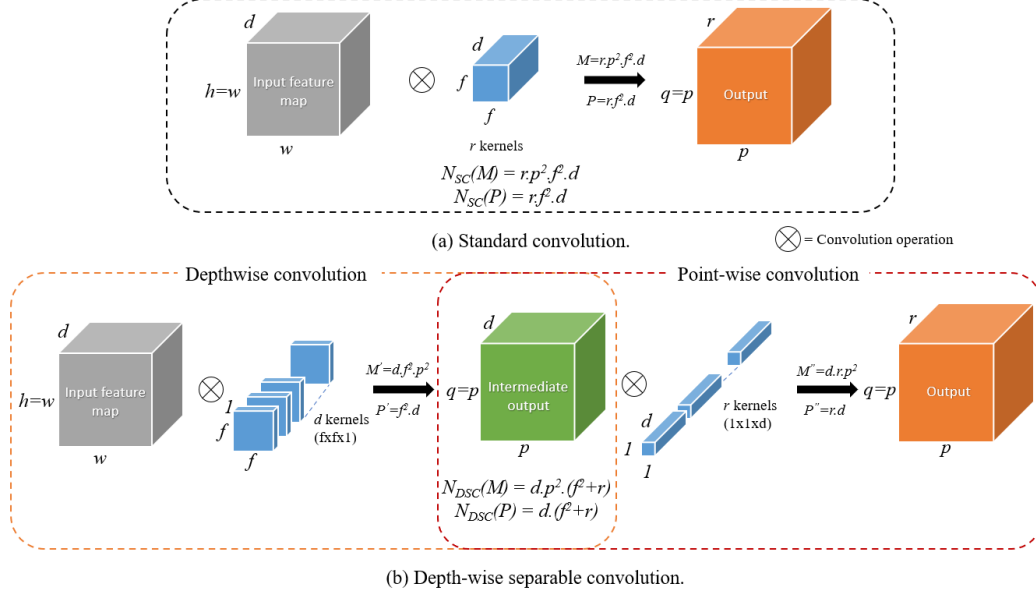


Figure 4: Standard convolution operation vs depthwise separable convolution operation.

to its symmetrical encoder-decoder framework divided into contraction and expansion path, the model can extract low and high-level features at the varying hierarchy of resolutions, and reconstruct the output segmentation map in the desired dimensions.

Following this, many variations of U-Net have been proposed [18, 19, 20, 21]. In most of the extended versions of U-Net, the feature maps produced in contraction phase are preprocessed via attention gates (AG) [22], squeeze and excitation block (SE) [23], spatial and channel SE blocks [24], etc., before concatenating with the corresponding expansion layer. It has also been observed that to segment regions of varying shapes and size require different sizes of receptive field [25]. Since, the COVID-19 infected regions may vary in shape, size and location, the present article incorporates the proposed inception block into the standard U-Net. Furthermore, to improve the computational power, the proposed approach also integrates depthwise separable convolution (DSC) layers [26], divided into two stages: depthwise and point-wise convolutions. Fig. 4 draws the contrast between standard convolution (SC) and DSC for some feature map,  $\mathcal{F} \in \mathbb{R}^{w \times h \times d}$ , where  $w$  is width,  $h$  is

height and  $d$  is depth of the input. It is observed that DSC reduces the number of multiplications (M) and parameters (P) than the SC as given by the Eq. 1. This significantly reduces the training time and computational cost without affecting the performance of the model.

$$\frac{N_{DSC}}{N_{SC}} = \frac{1}{r} + \frac{1}{f^2} \quad (1)$$

where  $N_{DSC}$  and  $N_{SC}$  indicates number of parameters or multiplications in depthwise separable convolution and standard convolution respectively,  $r$  is the depth of the output volume and  $f$  indicates dimension of the kernel as shown in Fig. 4.

### 1.3. Why hierarchical segmentation?

The present article addresses the challenging problem of efficiently identifying the COVID-19 infected regions in the CT images. Since these infected regions are present inside the lungs, the information present outside the lungs area becomes irrelevant. Therefore, in the proposed approach instead of direct segmentation, a hierarchical segmentation approach is introduced. In hierarchical segmentation, two residual attention inception U-Net (RAIU-Net) models are cascaded where the first model extracts lungs region from the CT images to generate the lungs contour feature maps and the second model utilizes these maps to segment the COVID-19 infected areas. Later, with the extensive trials, it was observed that the hierarchical segmentation approach significantly outperformed the direct segmentation scheme and also advanced the recently proposed approaches for COVID-19 segmentation.

### 1.4. Challenges addressed

COVID-19 infection segmentation in CT images is a challenging task due to the following concerns:

1. The presence of high variation in pattern, area and locale of infections in CT slices makes it difficult to segment. For instance, small infected regions can easily get neglected by the model which increases the false-negative predictions. This challenge is addressed by proposing inception convolution blocks that follow depthwise separable convolutions (DSC) of varying filter sizes ( $2 \times 2$ ,  $3 \times 3$ ,  $5 \times 5$ ) and a hybrid pooling layer accompanied with batch normalization and rectified linear unit activation.

2. Limited data availability of the COVID-19 infected patients, resulting due to privacy and security concerns. This affects the training of deep learning models. This challenge is addressed by the segmentation loss function and fusion of publicly accessible multiple datasets of CT volumes consisting of coronavirus and non-coronavirus slices to generate a large volume of data.
3. The intensity variance between the infected regions and background (regions outside the lungs area) is small, this restricts the deep learning models to identify the infected regions efficiently. This challenge is tackled by proposing a hierarchical segmentation approach where the irrelevant background is discarded before the identification of COVID-19 infection by generating lungs contour maps; later these contours are utilized to efficiently detect the infected regions.
4. The proposed CHS-Net model is a deep network, where the deep networks suffer from performance degradation due to the problem of vanishing and exploding gradient. To address this problem, each block of RAIU-Net model is equipped with residual (skip) connections to improve the flow of information in the network.

#### 1.5. *Our contribution*

This article presents the following contribution in the COVID-19 infectious image segmentation research:

1. A novel deep learning hierarchical approach, CHS-Net, built using RAIU-Net, is proposed for segregating the coronavirus infected areas using CT scans by exploiting the potential strategies of the state-of-the-art deep learning models.
2. A residual inception module is incorporated with a U-Net model to efficiently decode the semantic and varying resolution information considering the features extracted at each layer of the contraction phase to generate infection segmentation.
3. A hybrid of max pooling and spectral pooling is proposed for the efficient reduction in the spatial dimension of the feature maps with minimal loss of information.
4. A skip connection based on spectral spatial and depth attention (SSD) mechanism is proposed that uses global spectral pooling to infer the inter-spatial and channel features correlations for the effective flow of feature maps between the contraction and expansion phases.

5. A fusion dataset is introduced with 3560 CT slices, developed using COVID-19 CT segmentation nr.2 dataset [27] and COVID-19 CT lung and infection segmentation dataset [28]. Each CT slice has the corresponding lungs mask and COVID-19 infection mask. The code and dataset will be released at the github repository.

### *1.6. Article organization*

The rest of the paper is presented in various sections involving a literature survey in the related work section which highlights the recent findings and approaches for COVID-19 detection via CT medical imaging. The later section discusses the proposed approach to effectively identify and segregate the COVID-19 infected regions in the lungs. Furthermore, the experimental and results section describes the obtained results along with the exhaustive experimental trials and comparative analysis, dataset description and ablation study. The final section highlights the concluding remarks and further possible extensions of the work.

## **2. Related work**

With rapid advancements in technology, many artificial intelligence driven solutions are being developed to fight against COVID-19 pandemic [29]. In recent studies [30, 31, 32], CT abnormalities corresponding to COVID-19 are being utilized by practitioners and doctors. It is observed that CT scan highlights discrete patterns to identify the infected patients even at the initial stages, making automatic CT medical imaging analysis a promising area of research among the research community [32]. It is also observed that CT diagnosis for COVID-19 abnormality detection can be carried before the appearance of clinical symptoms [16]. Hence, many research works have been proposed for automatic early detection with classification and segmentation of the COVID-19 infection from CT scans [33, 34].

Li et al. [35] proposed a fully automatic CNN based COVID-19 detection neural network (COVNet), to classify COVID-19 abnormalities from community acquired pneumonia (CAP) and normal cases using chest CT imaging. The authors achieved 96% area under the receiver operating characteristic curve (AUC-ROC) to identify COVID-19 cases and performed better than RT-PCR testing. Even after achieving good results, the authors claimed that the proposed approach is not sufficient to segregate and classify different



types of pneumonia due to the limited data availability. Butt et al. [36] proposed deep learning based COVID-19 screening system to distinguish corona infected samples from non-corona samples. The proposed system yielded faster detection rate than RT-PCR testing with an overall accuracy score of 86.7%. Shan et al. [13] proposed V-Net [37] based deep learning model to segment and quantify the COVID-19 infected regions. The authors achieved a dice similarity index of  $91.6\% \pm 10.0\%$  between manual and deep learning enabled automatic delineation. However, these approaches do not provide localized information about the infected regions in the CT scan of the lungs.

A multistage deep learning framework is proposed by Gozes et al. [38] that follows segmentation to remove the irrelevant regions and classification of segmented regions into coronavirus infected and other viral pneumonia. For segmentation, the U-Net [17] model is utilized to acquire the relevant regions and then a pretrained ResNet-50 [39] model is fine-tuned to classify COVID-19 infected samples. Yan et al. [40] proposed COVID-SegNet accompanied with feature variation block and progressive atrous convolutions to highlight the diverse infected regions along with the boundaries. The proposed approach achieved a dice score of 0.726 for COVID-19 segmentation. Furthermore, Hu et al. [41] developed an object detection based approach to highlight the infected region with the help of the bounding boxes. The authors followed a weakly supervised approach to improve model performance with a limited number of labelled COVID-19 samples. The authors employed VGG model variants to classify COVID-19 from CAP and non-pneumonia cases. In similar work, Fan et al. [12] proposed lung infection segmentation deep network (Inf-Net) to segment COVID-19 infected regions with ground glass opacities (GGO) and consolidation while also addressing the challenges of high variation characteristics and low intensities of the abnormalities, and limited availability of the infected samples. With extensive trials, Inf-Net outperformed the recently proposed approaches. Following from these notions the present article contributes towards further improvement in the COVID-19 segmentation performance by introducing a hierarchical segmentation approach that generates lungs contour maps to efficiently segment the coronavirus infected regions.

### 3. Proposed network

The proposed COVID-19 hierarchical segmentation network (CHS-Net), as shown in Fig. 5, is inspired from the state-of-the-art deep learning archi-

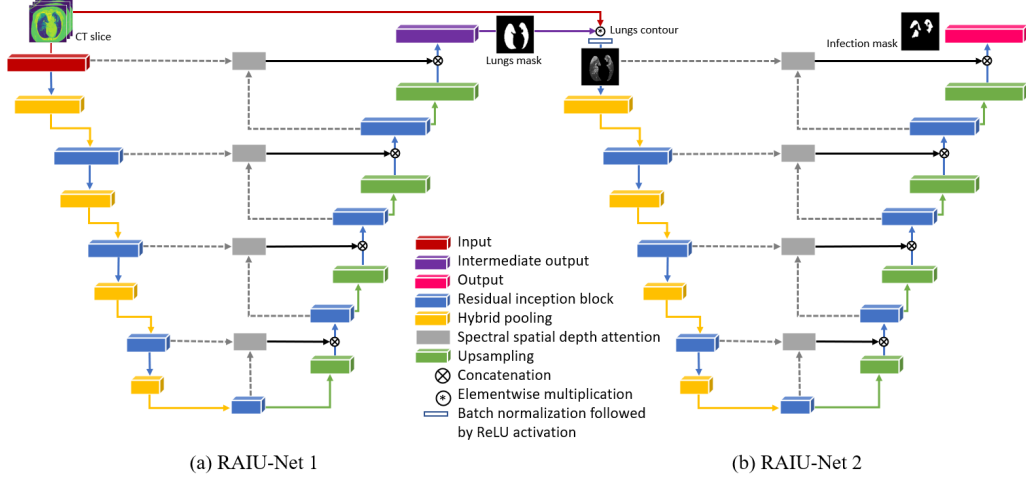


Figure 5: Schematic representation of CHS-Net (a) generates lungs contour maps, (b) generates infected regions.

tectures: U-Net [17], Google’s inception model [42], residual network [39] and attention strategy [22]. For hierarchical segmentation, two RAIU-Net models are connected in a series where the first model generates lungs contour maps Fig. 5(a) and then the second model utilizes these maps to identify the infected regions Fig. 5(b). The depth of the model is divided into four stages where each stage extract feature maps at different spatial dimensions. In contraction phase each stage reduces the width and height by 50%, and increase depth by 50% and vice-versa in the expansion phase.

Fig. 6 presents the schematic representation of the building block of RAIU-Net for some input feature map,  $\mathcal{F} \in \mathbb{R}^{w \times h \times d}$ . RAIU-Net model is developed in a U-Net fashion where each 2D convolution is replaced with inception blocks (concatenated  $1 \times 1$ ,  $3 \times 3$  and  $5 \times 5$  DSCs, and hybrid pooling followed by batch normalization to reduce the internal covariance shift and rectified linear unit as activation) while following the residual learning approach. The residual function reformulates the layer as learning in correspondence to the layer input. The extracted features from each residual inception block (RIB) are concatenated with corresponding transposed convolutions [43] representing similar spatial dimensions in the expansion phase, using skip connections [44]. Instead of direct concatenation, these skip connections are equipped with spectral spatial and depth attention (SSD) net-

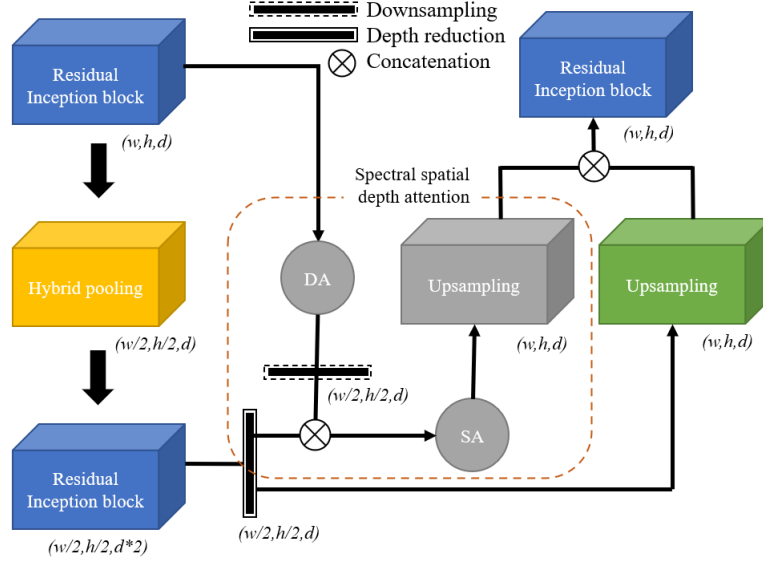


Figure 6: Building block of RAIU-Net.

work to process the extracted feature maps and preserve the most relevant high or low-level feature maps. The dimension inconsistency of the concatenating layers is removed using strided convolution to reduce spatial dimensions and  $1 \times 1$  convolution to reduce the depth, as shown in Fig. 6. Finally, the sigmoid activated  $1 \times 1$  convolution outputs the lungs contour map along with segmented regions of COVID-19 abnormalities.

### 3.1. Residual inception block

Fig. 7 presents the schematic representation of the RIB for some input feature map,  $\mathcal{F}_i \in \mathbb{R}^{w \times h \times d}$ . It is developed using double inception convolution with a shortcut connection from the input to the output layer. The shortcut or residual connection follows  $3 \times 3$  DSC whose batch normalized output is merged with the output of the double inception convolution ( $IC_1$  and  $IC_2$ ) to extract feature maps using  $d'$  number of filters. The consecutive RIBs are connected with the help of valid hybrid pooling which reduces the dimensions of feature maps while preserving the prominent features to produce feature map,  $\mathcal{F}_o \in \mathbb{R}^{w/2 \times h/2 \times d'}$ .

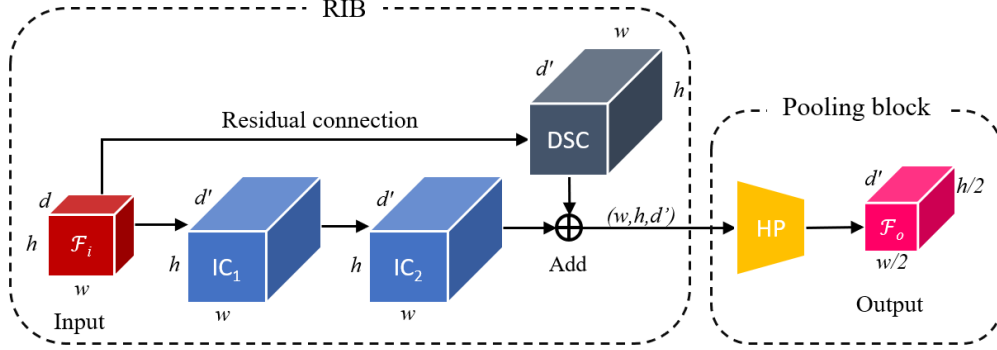


Figure 7: Schematic representation of the residual inception block.

### 3.1.1. Hybrid pooling

Many pooling variants have been proposed based on the value, rank, probability and domain transformation [45], among which spectral pooling is found to preserve more spatial information while also reducing the dimensions. Max pooling is featured in every deep learning architecture, however, it only preserves the sharpest features of an image. Whereas the spectral pooling is one of the domain transformation based variants that tend to preserve more information and also reduces the dimensions. Fig. 8 presents the comparison of max pooling and spectral pooling for varying filter sizes as  $2 \times 2$ ,  $8 \times 8$ ,  $16 \times 16$  and  $64 \times 64$  on randomly selected CT slice.

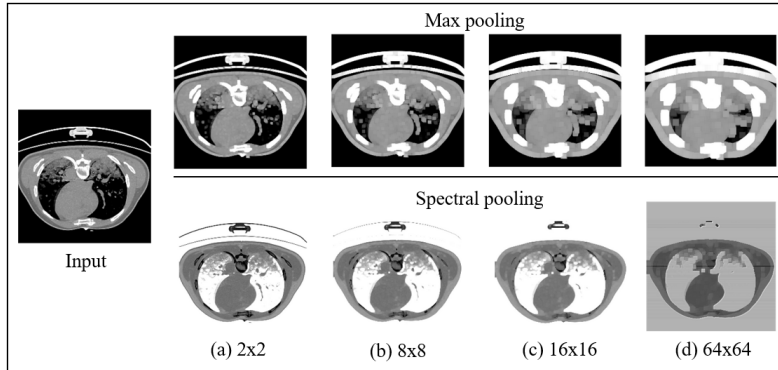


Figure 8: Downsampling using max and spectral pooling with the factors (a)  $2 \times 2$ , (b)  $8 \times 8$ , (c)  $16 \times 16$  and (d)  $64 \times 64$ .

In spectral pooling 2D discrete Fourier transform (DFT) of the input image,  $\mathcal{I}_{w,h,d}$ , is computed as shown in Eq. 2 (concatenated over depth  $d$ ), providing the frequency maps shifted to the center DC component to truncate the high frequency [46]. Finally, the inverse DFT is computed to map the filtered frequency back into the spatial domain, where inverse DFT can be computed as a conjugate of the DFT as  $DFT^{-1}(\cdot) = DFT(\cdot)^*$ .

$$DFT(\mathcal{I}_{w,h,d})_{mn} = \bigcup_d \frac{1}{\sqrt{wh}} \sum_{j=0}^{w-1} \sum_{k=0}^{h-1} \mathcal{I}_{jkd} e^{-2\pi i(\frac{jm}{w} + \frac{kn}{h})} \quad (2)$$

$$\forall m \in \{0, \dots, w-1\}, \forall n \in \{0, \dots, h-1\}$$

where  $\bigcup_d$  indicates concatenation of  $DFT$  of each feature map along the channel axis.

In the present article, a hybrid pooling ( $\mathcal{P}_h$ ) approach is proposed to leverage the features of both spectral and max pooling. In this, an input image undergoes spectral and max pooling in parallel followed by  $1 \times 1$  convolution. This can be performed to generate output with either valid or same padding.

### 3.1.2. Inception convolution

It is observed that each feature extraction and reconstruction phase requires different filter sizes to recognize regions or objects of varying dimensions, locale and area. The inception convolution comprises parallel DSCs with filter sizes  $1 \times 1$ ,  $3 \times 3$  and  $5 \times 5$ , and hybrid pooling accompanied with batch normalization (BN) (faster convergence and reduce covariance shift) and rectified linear unit (ReLU) activation function (adds non-linearity) to extract multi-level features for the same instance. The extracted feature maps are then concatenated using  $1 \times 1$  convolution to optimize the cross channel correlation without considering or modifying the spatial dimensions, followed by BN and ReLU. Fig. 9 describes the schematic representation of the inception convolution that acts as a basis of the RIB.

For an input feature map,  $\mathcal{F}_i \in \mathbb{R}^{w \times h \times d}$ , the inception convolution operation can be represented as in Eq. 3.

$$IC(\mathcal{F}_i) = \left( \mathcal{K}_{1 \times r} * \left( \left( \bigcup_{f \in (1,3,5)} (\mathcal{K}_{f \times r} * \mathcal{F}_i)_{p,q,r} \right) \bigcup \mathcal{P}_h(\mathcal{F}_i) \right) \right)_{p,q,r} \quad (3)$$

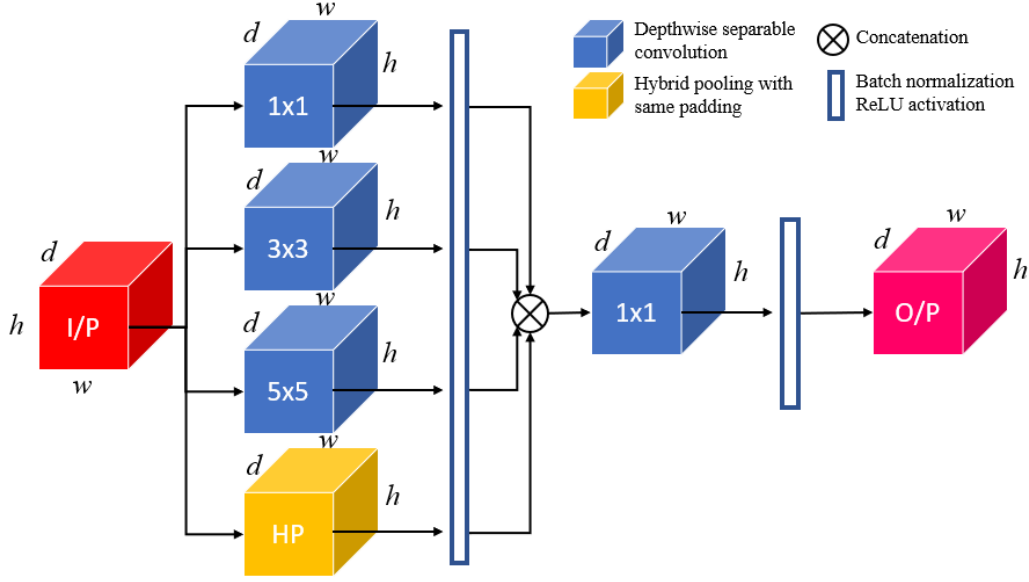


Figure 9: Design of inception convolution (IC).

$$(\mathcal{K}_{f \times r} * \mathcal{F}_i)_{p,q,r} = \max \left( \text{BN} \left( \text{DSC}(\mathcal{K}, \mathcal{F}_i)_{p,q,r} \right), 0 \right) \quad (4)$$

$$\text{DSC}(\mathcal{K}, \mathcal{F})_{p,q,r} = \sum_i^r \mathcal{K}_i \cdot \mathcal{F}_{(p,q,i)} \left( \bigcup_d \sum_{j,k}^{w,h} \mathcal{K}_{(j,k,d)} \odot \mathcal{F}_{(j+p,k+q,d)} \right) \quad (5)$$

where  $\bigcup$  indicates concatenation of feature maps along channel axis and  $\odot$  indicates element-wise product.  $\mathcal{K}_{f \times r}$  represents a kernel or a filter with dimensions  $(f \times f \times d \times r)$  ( $r$  indicates number of filters and  $d$  indicates same depth of the kernel as input),  $(\mathcal{K}_{f \times r} * \mathcal{I})_{p,q,r}$  (shown in Eq. 6) indicates a transformed image with features mapping from dimension as  $w \times h \times d \mapsto p \times q \times r$  by utilizing the DSC that follows from pointwise convolution operation of the depthwise convolved feature maps. The output dimension,  $D_o(p, q, r)$  can be computed as shown in Eq. 7.

$$(\mathcal{K}_{f \times r} * \mathcal{I})_{p,q,r} = \bigcup_r \sum_{i=1}^w \sum_{j=1}^h K_{i,j} I_{p+i,q+j} \quad (6)$$

$$D_o(p, q, r) = \left( \left\lfloor \frac{w + 2p - f}{s} + 1 \right\rfloor, \left\lfloor \frac{h + 2p - f}{s} + 1 \right\rfloor, r \right); s > 0 \quad (7)$$

where  $s$  and  $p$  denotes the amount of strides and padding respectively.

### 3.2. Spectral spatial and depth attention

The attention map aids the network to selectively process the information instead of complete volume by utilizing the inter spatial and channel features correlations. To the best of our knowledge, so far the attention map is obtained by applying either global average pooling or global max pooling, or both [47, 48]. However, it is evident that these pooling operations tend to be biased towards extreme features (pixels with high intensity). Therefore, a global spectral pooling layer is employed into the attention mechanism to extract most prominent features and generate the attention descriptors,  $\mathcal{A}_s^{w \times h \times 1}$  (spatial) and  $\mathcal{A}_d^{1 \times 1 \times d}$  (depth), that infers distinctive object features for an input volume  $\mathcal{F}_i$ . Finally, these attention descriptors undergo element-wise multiplication with the  $\mathcal{F}_i$  followed by ReLU activated  $1 \times 1$  convolution and BN, to produce refined volumes.

#### 3.2.1. Spectral depth attention

The operation of spectral depth attention approach is described in Fig. 10. The input feature maps,  $\mathcal{F}_i \in \mathbb{R}^{m \times n \times p}$  undergoes global spectral pooling ( $\mathcal{P}_{gsp}$ ) to generate  $\mathcal{F}_{gsp} \in \mathbb{R}^{1 \times 1 \times p}$ . The resulting flattened features pass through the shallow convolution neural network (SCNN). The network comprises of two blocks of  $1 \times 1$  ReLU activated convolutions to generate depth attention descriptor  $\mathcal{A}_d \in \mathbb{R}^{1 \times 1 \times p}$  as shown in Eq. 8. The attention descriptor,  $\mathcal{A}_d$  then undergoes element-wise multiplication with  $\mathcal{F}_i$ , followed by batch normalization and ReLU activation to produce spectral depth attention volume  $\mathcal{F}_d \in \mathbb{R}^{m \times n \times p}$  as shown in Eq. 9.

$$\mathcal{A}_d = (\mathcal{K}_{1 \times p} * (\mathcal{K}_{1 \times p/2} * \mathcal{P}_{gsp}(\mathcal{F}_i)))_{1,1,p} \quad (8)$$

$$\mathcal{F}_d = (\mathcal{K}_{1 \times p} * (\mathcal{A}_d \odot \mathcal{F}_i))_{m,n,p} \quad (9)$$

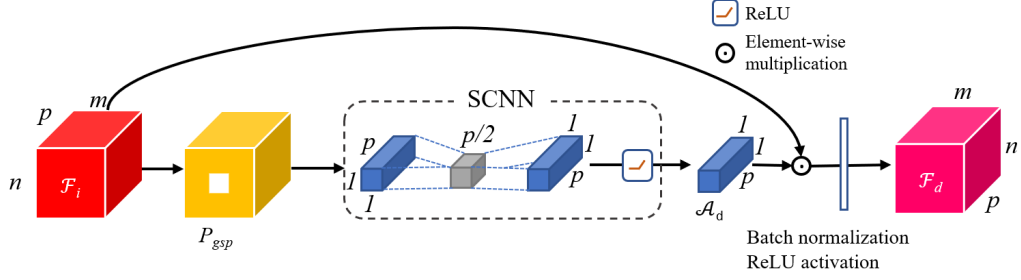


Figure 10: Representaiton of spectral depth attention network architecture.

### 3.2.2. Spectral spatial attention

The overall approach is illustrated in Fig. 11. For some feature map at layer  $l$ ,  $\mathcal{F}_i^l \in \mathbb{R}^{m \times n \times p}$ , the spectral spatial attention takes the input as  $\mathcal{F}_i^l$  and spectral depth attention of the previous layer feature map,  $\mathcal{F}_d^{l-1}(\mathcal{F}_i^{l-1})$ , where  $\mathcal{F}_i^{l-1} \in \mathbb{R}^{2m \times 2n \times p/2}$ . The operation starts with the two-strided convolution of  $\mathcal{F}_i^{l-1}$  such that it downsamples to  $\mathcal{F}' \in \mathbb{R}^{m \times n \times p}$  which is then merged with the  $1 \times 1$  convolution of  $\mathcal{F}_i^l$  following the BN and ReLU activation function indicated as  $\gamma$  in Eq. 10. Later, spatial attention descriptor,  $\mathcal{A}_s \in \mathbb{R}^{2m \times 2n \times 1}$  is generated by upsampling the ReLU activated  $1 \times 1$  convolution of the  $\gamma$  as shown in Eq. 11. Finally, similar to the spectral depth attention,  $\mathcal{A}_s$  is element-wise multiplied with  $\mathcal{F}_d^{l-1}$  accompanied with  $1 \times 1$  convolution and batch normalization to form spectral spatial attention volume,  $\mathcal{F}_s \in \mathbb{R}^{2m \times 2n \times p/2}$  as shown in Eq. 12.

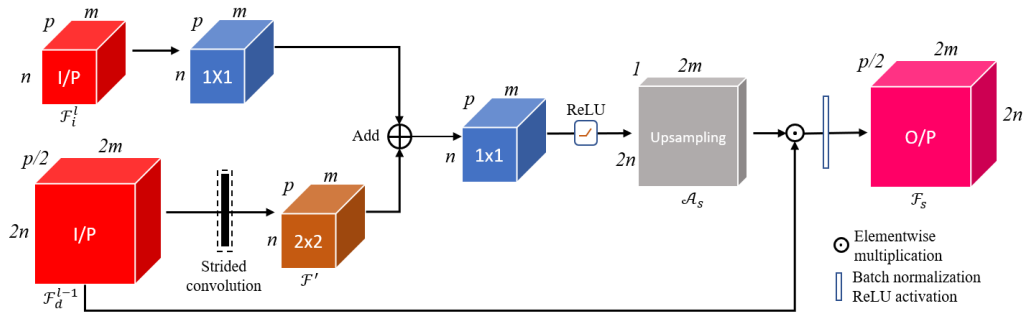


Figure 11: Representaiton of spectral spatial attention network architecture.



$$\gamma = (\mathcal{K}_{2 \times p} * \mathcal{F}_d^{l-1}) + (\mathcal{K}_{1 \times p} * \mathcal{F}_i^l) \quad (10)$$

$$\mathcal{A}_s = (Up(\sigma(\mathcal{K}_{1 \times p} * \gamma)))_{2m, 2n, 1} \quad (11)$$

$$\mathcal{F}_s = (\mathcal{K}_{1 \times p/2} * (\mathcal{A}_s \odot \mathcal{F}_d^{l-1}))_{2m, 2n, p/2} \quad (12)$$

### 3.3. Objective function

The CHS-Net is trained with the segmentation loss function  $\mathcal{L}$  defined as the weighted average of binary cross-entropy loss ( $BCL$ ) and dice loss ( $DL$ ). The segmentation task can be treated as a binary classification task to classify each pixel either belonging to the background (negative) or the region of interest (positive).

The binary cross entropy as defined in Eq. 13 is the most widely used loss function for binary classification and works effectively if there are equal distributions of positive and negative samples.

$$BCL(y, p(y)) = - \sum_i^N (y_i \cdot \log(p(y_i)) + (1 - y_i) \cdot \log(1 - p(y_i))) \quad (13)$$

where  $N$  indicates total number of pixels in an image  $\mathcal{I}$ ,  $y_i$  and  $p(y_i)$  presents the ground truth value and predicted value of  $i^{th}$  pixel respectively.

However, due to fewer infectious pixels in CT images, standalone binary cross entropy is not sufficient. Therefore to better penalize the false positive and negative predictions, dice loss is also utilized, defined in Eq. 14. The  $DL$  tends to equally penalize the false negative (FN) and false positive (FP) predictions.

$$DL(y, p(y)) = 1 - \frac{2 \sum_i^N y_i \cdot p(y_i)}{\sum_i^N |y_i|^2 + \sum_i^N |p(y_i)|^2} \quad (14)$$

The overall loss function  $\mathcal{L}$  is represented by Eq. 15.

$$\mathcal{L}(\mathcal{I}, p(\mathcal{I})) = \frac{1}{2} BCL(y, p(y)) + \frac{1}{2} DL(y, p(y)) \quad (15)$$

Table 1: CT slices distribution details in the synthesized fused dataset.

Dataset	No. of CT Volumes	Dimension	Fused dataset		
			No. of CT slices	No. of Lungs mask	No. of COVID-19 infection mask
COVID-19 CT segmentation nr. 2 [27]	9	630x630xd*	3560	3560	2200
COVID-19 CT lung and infection segmentation [28]	20	630x630xd* 512x512xd*			

\*d indicates that the number of slices varies for each volume

## 4. Experimentation and results

### 4.1. Dataset description

The CHS-Net is trained and evaluated on the synthesized dataset generated using publicly available COVID-19 CT segmentation datasets [27, 28]. This dataset source [27] is the only open-access data repository that has COVID-19 CT segmentation datasets because of government norms and personal privacy. These two datasets are merged to form an aggregated dataset that addresses the problem of limited availability of the COVID-19 data. The fused dataset consists of 3560 CT slices with dimensions as  $256 \times 256 \times 1$ , each having associated lungs mask and COVID-19 infection mask. Table 1 highlights the class summary details of the fused dataset. The CT slices with just black or dark pixels were irrelevant and hence filtered out. In the fused dataset, for each CT slice, there are corresponding lungs mask, but not COVID-19 mask due to the absence of infection and hence are represented with set of dark pixels of dimension  $256 \times 256 \times 1$ .

These 2D CT slices are extracted from the 29 3D volumes of the CT imaging having non-uniform or varying dimensions, resized to  $256 \times 256 \times 1$ . Each of these slices is annotated carefully by expert radiologists to generate the segmentation mask. Fig. 12 shows the sample slices along with the ground truth segmentation mask corresponding to the lungs and COVID-19 infected region. Each pixel of the slices is marked with class labels as 1 or 0 where 1 means the pixel belongs to the region of interest that is associated with lungs in lungs annotation and COVID-19 (GGO and consolidations) in infection annotation, and 0 means the background.

### 4.2. Training and testing

The training and testing sets are acquired from the fused dataset to train and evaluate the proposed CHS-Net. The training and test sets comprises

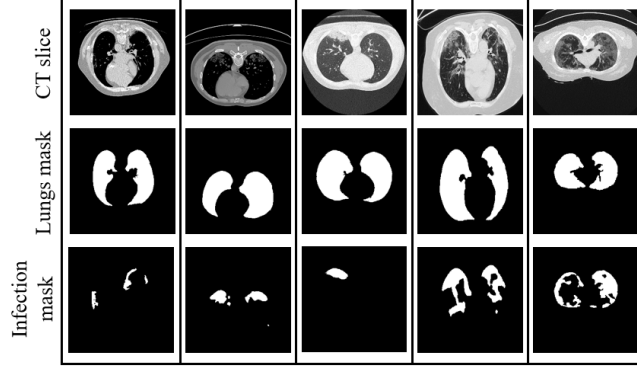


Figure 12: CT slices and corresponding ground truth masks from the fused dataset.

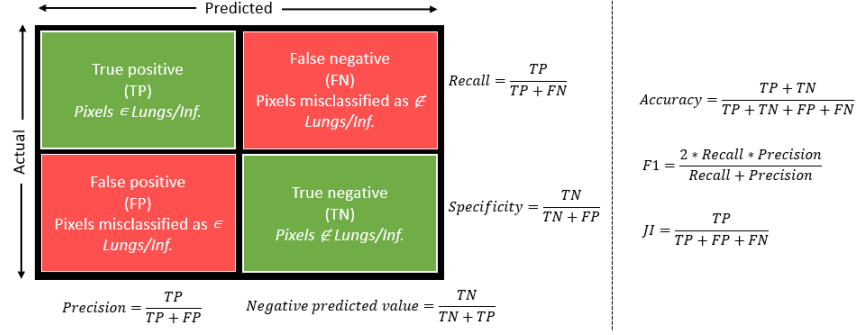


Figure 13: Confusion matrix and evaluation metrics.

70% and 30% of the samples respectively. The training phase of the CHS-Net is assisted with stochastic gradient descent (SGD) as training weights optimizer to minimize the segmentation loss function (objective function), Adam as a learning rate optimizer [49], 5-fold cross validation for robustness, and early stopping to avoid the overfitting problem [50] techniques on the high performance computing environment with Nvidia RTX Titan GPUs. The trained model is evaluated with the help of a test set in terms of accuracy, precision, recall, specificity, F1 score (dice coefficient) and Jaccard index (intersection over union). Fig. 13 describes the confusion matrix that can be generated for the predicted mask corresponding to the CT slice to compute the above discussed metrics based on the correct prediction: true positive (TP), true negative (TN) and incorrect prediction: false positive (FP), false negative (FN).

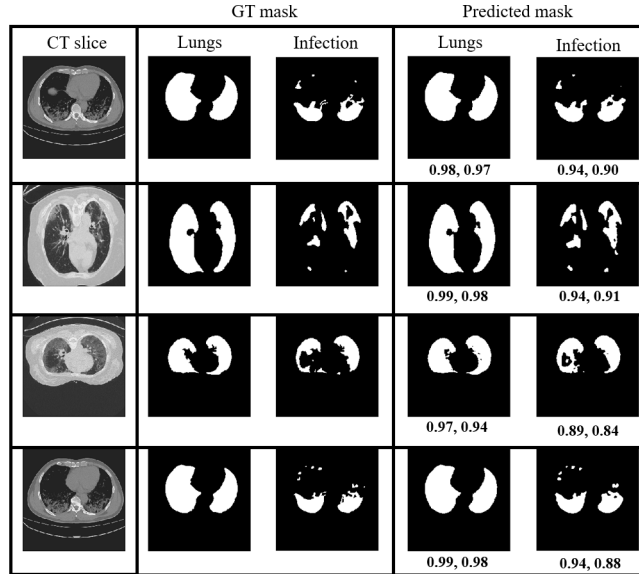


Figure 14: Qualitative results of COVID-19 infection segmentation on test set obtained from fused dataset. The quantities indicate the dice score and Jaccard index values respectively, for each generated mask.

Table 2: Quantitative results of the CHS-Net on the test set generated from fused dataset.

Segmentation	Acc.	Pre.	Spe.	Rec.	DSC	JI
Lungs	0.99	0.97	0.99	0.95	0.96	0.98
COVID-19	0.96	0.85	0.97	0.92	0.88	0.96

#### 4.3. Results and discussion

The proposed model generates the semantic segmentation mask of the COVID-19 infected regions in the lungs based on the generated lungs contour maps. Fig. 14 presents the qualitative results of CHS-Net over randomly chosen CT axial slices. This visual representation and the obtained evaluation metrics scores indicate that the results match the ground truth masks and hence effectively detects and localize the coronavirus infected regions. Table 2 discusses the results of the proposed model (CHS-Net) in terms of accuracy (Acc.), precision (Pre.), specificity (Spe.), recall (Rec.), dice coefficient (DSC), and Jaccard index (JI) for hierarchical semantic segmentation of COVID-19 infectious images following from the lungs segmentation.

Furthermore, the obtained results are compared with the recently pro-

Table 3: Comparative analysis of the CHS-Net with recently proposed approaches.

Model	Parameters	Infection segmentation					
		Acc.	Pre.	Spe.	Rec.	DSC	JI
MiniSeg [52]	472K	-	-	0.97	0.84	0.77	0.82
U-Net based model [51]	-	-	-	<b>0.99</b>	0.87	0.83	-
Inf-Net [12]	33M	-	-	0.94	0.69	0.68	-
Semi-Inf-Net [12]	33M	-	-	0.96	0.73	0.74	-
CHS-Net	4.2M	<b>0.96</b>	<b>0.85</b>	0.97	<b>0.92</b>	<b>0.88</b>	<b>0.96</b>

\*bold quantities indicate highest scores

posed approaches, as shown in Table 3. It is observed that CHS-Net approach outperformed the other approaches with significant improvement in the evaluation metrics values. However, among these evaluation metrics, precision is obtained with the least value, indicating that model generates approximately 15% of false positive predictions from the pool of test set, which is comparatively less than other approaches but leaves the void for further improvements. In addition, model proposed by Zhou et al. [51] slightly achieves better specificity score of 99%, however limited COVID-19 infected samples were utilized [27]. Moreover, unlike our fused dataset, the other approaches train and evaluate their respective approaches on limited samples and hence results are not robust.

In contrast, the success of the CHS-Net follows from its hierarchical segmentation strategy executed via proposed cascaded RAIU-Net model, where instead of directly segmenting the COVID-19 infected regions, lungs contour maps are generated from the predicted lungs mask which then serve as the input to another RAIU-Net model for localizing the infected regions. Moreover, in CHS-Net, spectral representations (hybrid pooling and global spectral pooling) are employed that aids in efficiently downsampling the feature maps with least loss of information. Furthermore residual inception blocks tends to efficiently encode and decode the semantic and varying resolution information. In addition, the adopted SSD mechanism refines the high and low extracted feature maps that are later merged in the reconstruction phase.

Furthermore, the significance of each component (RIB, HP and SSD) utilized in the proposed framework is presented in Table 4 and Table 5 with the help of the evaluation metrics to highlight their impact on the segmentation performance using the test set. Table 4 illustrates the ablation study

Table 4: Effects of the proposed components on the model performance for direct segmentation of COVID-19 infectious regions.

Mode	Infection segmentation					
	Acc.	Pre.	Spe.	Rec.	DSC	JI
BU	0.68	0.04	0.80	0.28	0.07	0.25
BU+RIB	0.75	0.55	0.90	0.35	0.43	0.50
BU+RIB+HP	0.88	0.63	0.95	0.68	0.65	0.68
BU+RIB+HP+SSD (RAIU-Net)	0.92	0.69	0.96	0.75	0.72	0.77

Table 5: Effects of the proposed components on the model performance for hierarchical segmentation of COVID-19 infectious regions.

Mode	Segmentation	Acc.	Pre.	Spe.	Rec.	DSC	JI
BU	Lungs	0.92	0.73	0.95	0.78	0.75	0.77
	Infection	0.75	0.21	0.80	0.32	0.25	0.28
BU+RIB	Lungs	0.98	0.85	0.98	0.88	0.86	0.90
	Infection	0.88	0.68	0.94	0.53	0.60	0.64
BU+RIB+HP	Lungs	0.98	0.91	0.99	0.92	0.91	0.94
	Infection	0.95	0.75	0.95	0.81	0.78	0.85
BU+RIB+HP+SSD (CHS-Net)	Lungs	0.99	0.97	0.99	0.95	0.96	0.98
	Infection	0.96	0.85	0.97	0.92	0.88	0.96

for direct COVID-19 infected region segmentation whereas Table 5 shows it for hierarchical segmentation (CHS-Net). This ablation study is carried under the same environment and comprises of baseline U-Net model (BU) [17] that follows standard convolutions and max pooling operations. Later, this model is extended with the proposed components as shown in Table 4 and Table 5 to highlight the significance of each component for achieving the concerned results. As observed in both the tables, even for baseline model the specificity metric value is significantly higher as compared to other metrics, indicating that model is predicting all pixels as background (dark) and hence not able to detect any infection, whereas with continuous incorporation of the proposed components the model tends to perform better in localizing the complex patterns associated with the infection. In addition, it is also observed that hierarchical segmentation approach works significantly better than direct segmentation, where each component certainly contributes for improvement in the model performance.

## 5. Conclusion

This article proposes a COVID-19 hierarchical segmentation network (CHS-Net) to identify the COVID-19 infected regions from the generated lungs contour maps with computed tomography (CT) images via cascaded residual attention inception U-Net (RAIU-Net) models. The RAIU-Net model improves upon the base U-Net model by exploiting various state-of-the-art components to improve the feature extraction and reconstruction process, where a residual inception block (RIB) and spectral spatial and depth attention (SSD) network tends to effectively encode and decode the feature maps at varying resolutions, while also addressing the major challenges involved in the segmentation. With extensive trials it was observed that the results of the CHS-Net model outperformed the other recently proposed approaches which were evaluated using standard benchmark performance metrics i.e. accuracy (96%), precision (85%), recall (92%), specificity (97%), F1 score (dice coefficient) (88%) and Jaccard index (intersection over union) (96%). The ablation study of the CHS-Net highlighted the contribution of each component towards the improvement in the segmentation results. Besides, trials can be made to tweak and tune the architecture with other deep learning components to further improve the results. It is believed that the potential of CHS-Net design can also be extended to other applications concerning biomedical image segmentation.

## Acknowledgment

We thank our institute, Indian Institute of Information Technology Allahabad (IIITA), India and Big Data Analytics (BDA) lab for allocating the centralised computing facility and other necessary resources to perform this research. We extend our thanks to our colleagues for their valuable guidance and suggestions.

## References

- [1] WHO, Who timeline - covid-19, <https://www.who.int/news-room/detail/08-04-2020-who-timeline---covid-19>, [Online; accessed December 10, 2020] (2020).
- [2] G. repository, 2019 novel coronavirus covid-19 (2019-ncov) data repository by johns hopkins csse, <https://github.com/CSSEGISandData/COVID-19>, [Online; accessed December 10, 2020] (2020).

- [3] WHO, Coronavirus disease 2019 (covid-19) situation report – 81, <https://www.who.int/docs/default-source/coronaviruse/situation-reports/>, [Online; accessed December 10, 2020] (2020).
- [4] N. S. Punna, S. K. Sonbhadra, S. Agarwal, Monitoring covid-19 social distancing with person detection and tracking via fine-tuned yolo v3 and deepsort techniques, arXiv preprint arXiv:2005.01385 (2020).
- [5] V. Rajinikanth, N. Dey, A. N. J. Raj, A. E. Hassanien, K. Santosh, N. Raja, Harmony-search and otsu based system for coronavirus disease (covid-19) detection using lung ct scan images, arXiv preprint arXiv:2004.03431 (2020).
- [6] P. Gómez, M. Semmler, A. Schützenberger, C. Bohr, M. Döllinger, Low-light image enhancement of high-speed endoscopic videos using a convolutional neural network, *Medical & biological engineering & computing* 57 (7) (2019) 1451–1463.
- [7] J. Choe, S. M. Lee, K.-H. Do, G. Lee, J.-G. Lee, S. M. Lee, J. B. Seo, Deep learning-based image conversion of ct reconstruction kernels improves radiomics reproducibility for pulmonary nodules or masses, *Radiology* 292 (2) (2019) 365–373.
- [8] N. S. Punna, S. Agarwal, Automated diagnosis of covid-19 with limited posteroanterior chest x-ray images using fine-tuned deep neural networks, arXiv preprint arXiv:2004.11676 (2020).
- [9] D. S. Kermany, M. Goldbaum, W. Cai, C. C. Valentim, H. Liang, S. L. Baxter, A. McKeown, G. Yang, X. Wu, F. Yan, et al., Identifying medical diagnoses and treatable diseases by image-based deep learning, *Cell* 172 (5) (2018) 1122–1131.
- [10] K. Li, Y. Fang, W. Li, C. Pan, P. Qin, Y. Zhong, X. Liu, M. Huang, Y. Liao, S. Li, Ct image visual quantitative evaluation and clinical classification of coronavirus disease (covid-19), *European radiology* (2020) 1–10.
- [11] D. Singh, V. Kumar, M. Kaur, Classification of covid-19 patients from chest ct images using multi-objective differential evolution-based convolutional neural networks, *European Journal of Clinical Microbiology & Infectious Diseases* (2020) 1–11.



- [12] D.-P. Fan, T. Zhou, G.-P. Ji, Y. Zhou, G. Chen, H. Fu, J. Shen, L. Shao, Inf-net: Automatic covid-19 lung infection segmentation from ct images, *IEEE Transactions on Medical Imaging* (2020).
- [13] F. Shan, Y. Gao, J. Wang, W. Shi, N. Shi, M. Han, Z. Xue, Y. Shi, Lung infection quantification of covid-19 in ct images with deep learning, *arXiv preprint arXiv:2003.04655* (2020).
- [14] T. Ai, Z. Yang, H. Hou, C. Zhan, C. Chen, W. Lv, Q. Tao, Z. Sun, L. Xia, Correlation of chest ct and rt-pcr testing in coronavirus disease 2019 (covid-19) in china: a report of 1014 cases, *Radiology* (2020) 200642.
- [15] M. Wadman, J. Couzin-Frankel, J. Kaiser, C. Maticic, How does coronavirus kill, Clinicians trace a ferocious rampage through the body, from brain to toes (2020) 1502–1503.
- [16] S. K. Jon-Emile, An illustrated guide to the chest ct in covid-19, <https://pulmccm.org/uncategorized/an-illustrated-guide-to-the-chest-ct-in-covid-19/>, [Online; accessed June 12, 2020] (2020).
- [17] O. Ronneberger, P. Fischer, T. Brox, U-net: Convolutional networks for biomedical image segmentation, in: *International Conference on Medical image computing and computer-assisted intervention*, Springer, 2015, pp. 234–241.
- [18] N. S. Punna, S. Agarwal, Inception u-net architecture for semantic segmentation to identify nuclei in microscopy cell images, *ACM Transactions on Multimedia Computing, Communications, and Applications (TOMM)* 16 (1) (2020) 1–15.
- [19] M. Z. Alom, M. Hasan, C. Yakopcic, T. M. Taha, V. K. Asari, Recurrent residual convolutional neural network based on u-net (r2u-net) for medical image segmentation, *arXiv preprint arXiv:1802.06955* (2018).
- [20] N. S. Punna, S. Agarwal, Multi-modality encoded fusion with 3d inception u-net and decoder model for brain tumor segmentation, *Multimedia Tools and Applications* (2020) 1–16.
- [21] Z. Zhou, M. M. R. Siddiquee, N. Tajbakhsh, J. Liang, Unet++: A nested u-net architecture for medical image segmentation, in: *Deep Learning in*

Medical Image Analysis and Multimodal Learning for Clinical Decision Support, Springer, 2018, pp. 3–11.

- [22] O. Oktay, J. Schlemper, L. L. Folgoc, M. Lee, M. Heinrich, K. Misawa, K. Mori, S. McDonagh, N. Y. Hammerla, B. Kainz, et al., Attention u-net: Learning where to look for the pancreas, arXiv preprint arXiv:1804.03999 (2018).
- [23] J. Hu, L. Shen, G. Sun, Squeeze-and-excitation networks, in: Proceedings of the IEEE conference on computer vision and pattern recognition, 2018, pp. 7132–7141.
- [24] A. G. Roy, N. Navab, C. Wachinger, Concurrent spatial and channel ‘squeeze & excitation’ in fully convolutional networks, in: International conference on medical image computing and computer-assisted intervention, Springer, 2018, pp. 421–429.
- [25] W. Luo, Y. Li, R. Urtasun, R. Zemel, Understanding the effective receptive field in deep convolutional neural networks, in: Advances in neural information processing systems, 2016, pp. 4898–4906.
- [26] F. Chollet, Xception: Deep learning with depthwise separable convolutions, in: Proceedings of the IEEE conference on computer vision and pattern recognition, 2017, pp. 1251–1258.
- [27] Covid-19 ct segmentation dataset nr. 2, <https://medicalsegmentation.com/covid19/>, [Online; accessed August 12, 2020] (2020).
- [28] Covid-19 ct lung and infection segmentation dataset, <https://zenodo.org/record/3757476#.X1nqY4vhWUn>, [Online; accessed August 12, 2020] (2020).
- [29] S. Agarwal, N. S. Pun, S. K. Sonbhadra, P. Nagabhushan, K. Pandian, P. Saxena, Unleashing the power of disruptive and emerging technologies amid covid 2019: A detailed review, arXiv preprint arXiv:2005.11507 (2020).
- [30] Y. Li, L. Xia, Coronavirus disease 2019 (covid-19): role of chest ct in diagnosis and management, American Journal of Roentgenology 214 (6) (2020) 1280–1286.

- [31] X. Ding, J. Xu, J. Zhou, Q. Long, Chest ct findings of covid-19 pneumonia by duration of symptoms, *European Journal of Radiology* (2020) 109009.
- [32] H. Meng, R. Xiong, R. He, W. Lin, B. Hao, L. Zhang, Z. Lu, X. Shen, T. Fan, W. Jiang, et al., Ct imaging and clinical course of asymptomatic cases with covid-19 pneumonia at admission in wuhan, china, *Journal of Infection* (2020).
- [33] F. Shi, J. Wang, J. Shi, Z. Wu, Q. Wang, Z. Tang, K. He, Y. Shi, D. Shen, Review of artificial intelligence techniques in imaging data acquisition, segmentation and diagnosis for covid-19, *IEEE reviews in biomedical engineering* (2020).
- [34] A. Shoeibi, M. Khodatars, R. Alizadehsani, N. Ghassemi, M. Jafari, P. Moridian, A. Khadem, D. Sadeghi, S. Hussain, A. Zare, et al., Automated detection and forecasting of covid-19 using deep learning techniques: A review, *arXiv preprint arXiv:2007.10785* (2020).
- [35] L. Li, L. Qin, Z. Xu, Y. Yin, X. Wang, B. Kong, J. Bai, Y. Lu, Z. Fang, Q. Song, et al., Artificial intelligence distinguishes covid-19 from community acquired pneumonia on chest ct, *Radiology* (2020).
- [36] C. Butt, J. Gill, D. Chun, B. A. Babu, Deep learning system to screen coronavirus disease 2019 pneumonia, *Applied Intelligence* (2020) 1.
- [37] F. Milletari, N. Navab, S.-A. Ahmadi, V-net: Fully convolutional neural networks for volumetric medical image segmentation, in: *2016 fourth international conference on 3D vision (3DV)*, IEEE, 2016, pp. 565–571.
- [38] O. Gozes, M. Frid-Adar, H. Greenspan, P. D. Browning, H. Zhang, W. Ji, A. Bernheim, E. Siegel, Rapid ai development cycle for the coronavirus (covid-19) pandemic: Initial results for automated detection & patient monitoring using deep learning ct image analysis, *arXiv preprint arXiv:2003.05037* (2020).
- [39] K. He, X. Zhang, S. Ren, J. Sun, Deep residual learning for image recognition, in: *Proceedings of the IEEE conference on computer vision and pattern recognition*, 2016, pp. 770–778.

- [40] Q. Yan, B. Wang, D. Gong, C. Luo, W. Zhao, J. Shen, Q. Shi, S. Jin, L. Zhang, Z. You, Covid-19 chest ct image segmentation—a deep convolutional neural network solution, arXiv preprint arXiv:2004.10987 (2020).
- [41] S. Hu, Y. Gao, Z. Niu, Y. Jiang, L. Li, X. Xiao, M. Wang, E. F. Fang, W. Menpes-Smith, J. Xia, et al., Weakly supervised deep learning for covid-19 infection detection and classification from ct images, IEEE Access (2020).
- [42] C. Szegedy, W. Liu, Y. Jia, P. Sermanet, S. Reed, D. Anguelov, D. Erhan, V. Vanhoucke, A. Rabinovich, Going deeper with convolutions, in: Proceedings of the IEEE conference on computer vision and pattern recognition, 2015, pp. 1–9.
- [43] V. Dumoulin, F. Visin, A guide to convolution arithmetic for deep learning, arXiv preprint arXiv:1603.07285 (2016).
- [44] M. Drozdal, E. Vorontsov, G. Chartrand, S. Kadoury, C. Pal, The importance of skip connections in biomedical image segmentation, in: Deep Learning and Data Labeling for Medical Applications, Springer, 2016, pp. 179–187.
- [45] N. Akhtar, U. Ragavendran, Interpretation of intelligence in cnn-pooling processes: A methodological survey, Neural Computing and Applications (2020) 1–20.
- [46] O. Rippel, J. Snoek, R. P. Adams, Spectral representations for convolutional neural networks, in: Advances in neural information processing systems, 2015, pp. 2449–2457.
- [47] S. Zagoruyko, N. Komodakis, Paying more attention to attention: Improving the performance of convolutional neural networks via attention transfer, arXiv preprint arXiv:1612.03928 (2016).
- [48] S. Woo, J. Park, J.-Y. Lee, I. So Kweon, Cbam: Convolutional block attention module, in: Proceedings of the European conference on computer vision (ECCV), 2018, pp. 3–19.
- [49] S. Ruder, An overview of gradient descent optimization algorithms, arXiv preprint arXiv:1609.04747 (2016).

- [50] R. Caruana, S. Lawrence, C. L. Giles, Overfitting in neural nets: Back-propagation, conjugate gradient, and early stopping, in: Advances in neural information processing systems, 2001, pp. 402–408.
- [51] T. Zhou, S. Canu, S. Ruan, An automatic covid-19 ct segmentation network using spatial and channel attention mechanism (2020). [arXiv:2004.06673](#).
- [52] Y. Qiu, Y. Liu, J. Xu, Miniseg: An extremely minimum network for efficient covid-19 segmentation (2020). [arXiv:2004.09750](#).